Journal of
Materials Chemistry A

ROYAL SOCIETY
OF CHEMISTRY

PAPER

View Article Online
View Journal

Check for updates

Cite this: DOI: 10.1039/d6ta02075e

Simultaneous enhancement of power factor and suppression of thermal conductivity in bulk $TlFe_{1.6}Se_2$ *via* embedded atomically thin FeSe layers

Xinyi He,†[ab] Katsuma Ogata,†[a] Terumasa Tadano, [c] Hidenori Hiramatsu,[ad]
Toshio Kamiya[ad] and Takayoshi Katase *[a]

FeSe in the monolayer limit exhibits extremely large thermoelectric power factors (PFs). Extending the high-PF concept from two-dimensional FeSe to bulk materials, together with the suppression of lattice thermal conductivity, enables higher-performance thermoelectrics. Here, layered $TlFe_{1.6}Se_2$ is identified as a model system consisting of atomically thin two-dimensional FeSe layers separated by Tl atoms; *i.e.*, FeSe monolayers are naturally confined within a bulk crystal. This compound uniquely exhibits a transition from Fe-vacancy (V_{Fe})-ordered to-disordered states at around 200 °C. Although the V_{Fe}-disordered phase exhibits high electrical conductivity, carrier compensation suppresses the Seebeck coefficient and limits PF. In contrast, the V_{Fe}-ordered phase shows an enhanced Seebeck coefficient associated with Mott gap formation, resulting in improved PF which is much higher than that of bulk FeSe. The lattice thermal conductivity of the V_{Fe}-ordered phase is lower than that of representative thermoelectric chalcogenides and that of the V_{Fe}-disordered phase further decreases to ~0.2 W (m^{-1} K^{-1}) at 500 °C due to the V_{Fe}-induced bond heterogeneity. Consequently, the dimensionless figure of merit (ZT) of $TlFe_{1.6}Se_2$ reaches ~0.2 at 50 °C in the V_{Fe}-ordered phase, which is two orders of magnitude higher than that of bulk FeSe. These results demonstrate that confining FeSe monolayers within a bulk crystal, alongside vacancy order–disorder control, is an effective design strategy for next-generation thermoelectrics.

Received 10th March 2026
Accepted 28th April 2026

DOI: 10.1039/d6ta02075e

rsc.li/materials-a

1 Introduction

Thermoelectric energy conversion is considered a promising renewable technology for converting waste heat into electricity *via* the Seebeck effect.[1–3] The energy-conversion efficiency of thermoelectric materials is governed by the dimensionless figure of merit (ZT), defined as $ZT = S^2\sigma T/\kappa$, where S is the Seebeck coefficient, σ is the electrical conductivity, T is the absolute temperature, and κ is the thermal conductivity. The electrical output power is given by $S^2\sigma$, known as the power factor (PF), and κ includes the electronic thermal conductivity (κ_{ele}) and lattice thermal conductivity (κ_{lat}). Achieving a high ZT requires simultaneously attaining a large S and high σ while minimizing κ. However, this requirement is fundamentally constrained by well-known trade-offs among these parameters. For example, σ and S exhibit an inverse dependence on the carrier concentration (n): increasing n enhances σ but reduces S, resulting in a maximum PF at an optimal n. Moreover, increasing σ typically raises κ_{ele} according to the Wiedemann–Franz law ($\kappa_{ele} = L\sigma T$, where L is the Lorenz number). Owing to this intricate interdependence of transport properties, realizing thermoelectric materials with high ZT remains a major challenge.[4] In contrast, κ_{lat} is largely independent of these electronic transport parameters, and materials with intrinsically low κ_{lat} are therefore well suited for achieving high ZT.

Recently, a giant PF has been reported in ultra-thin films of layered FeSe,[5] one of the high-critical-temperature (T_c) Fe-based superconductors.[6] Ultra-thin FeSe film grown on the $SrTiO_3$ substrate has attracted considerable research attention because it exhibits superconductivity with T_c up to 100 K,[7] dramatically higher than the bulk T_c of ~9 K. When the film thickness is reduced to ~1 nm, σ increases due to interface-induced carrier doping from the $SrTiO_3$ substrate, while S also increases due to the enhanced two-dimensionality and electron correlation effects. As a result, the PF reaches 260 μW (cm^{-1} K^{-2}), a value much higher than that of practical Bi_2Te_3 at room temperature (RT).[5] Furthermore, the PF of ultra-thin FeSe increases to 13 000 μW (cm^{-1} K^{-2}) at a reduced temperature of 50 K. Assuming $\kappa \approx$

---

[a] *Materials and Structures Laboratory, Institute of Integrated Research, Institute of Science Tokyo, 4259 Nagatsuta, Midori, Yokohama 226-8501, Japan. E-mail: katase.t.aa@m.titech.ac.jp*

[b] *Kanagawa Institute of Industrial Science and Technology, 705-1 Shimoimaizumi, Ebina, Kanagawa 243-0435, Japan*

[c] *Research Center for Magnetic and Spintronic Materials, National Institute for Materials Science, 1-2-1 Sengen, Tsukuba, Ibaraki 305-0047, Japan*

[d] *MDX Research Center for Element Strategy, Institute of Integrated Research, Institute of Science Tokyo, 4259 Nagatsuta, Midori, Yokohama 226-8501, Japan*

† X. H. and K. O. contributed equally to this work.

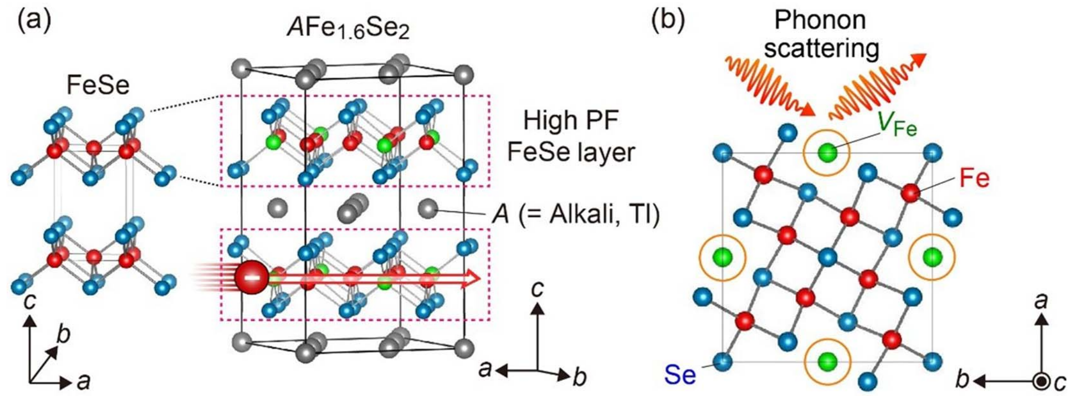

Fig. 1 Crystal structure of the layered $AFe_{1.6}Se_2$ (A = alkali metals and Tl) with an Fe-vacancy (V_{Fe}) ordered structure, viewed along the (a) [120] and (b) [001] directions. The spheres represent the Tl (gray), Fe (red), Se (blue) atoms, and V_{Fe} sites (green). The structure consists of FeSe layers, crystallographically equivalent to the high-power-factor (PF) FeSe monolayers, sandwiched by the A-ion layers. The Fe sites intrinsically host V_{Fe}, which undergo an order–disorder transition upon heating to ~500 K, which is expected to enhance phonon scattering. The coexistence of FeSe layers with intrinsic V_{Fe} defects is expected to enable a high PF, together with low lattice thermal conductivity.

5 W (m^{-1} K^{-1}), similar to bulk Fe-based superconductors,[8,9] the *ZT* of the ultra-thin FeSe is estimated to be ~1.5 at 280 K. However, the excellent PF and *ZT* values appear only in the ultra-thin limit, which makes these films unsuitable for thermoelectric power generation. It would therefore be more interesting to achieve such a high PF throughout the bulk phase of FeSe. In addition, FeSe has been reported to exhibit a relatively high $\kappa_{lat} \approx 4.5$ W (m^{-1} K^{-1}) at RT in polycrystalline samples,[10] which is nearly three times higher than that of Bi_2Te_3.[11] Therefore, reducing the κ_{lat} in FeSe is also crucial for realizing its potential as a high-performance thermoelectric material.

To overcome the limitations of ultra-thin FeSe, we herein focus on a layered $A_{1-x}Fe_{2-y}Se_2$ (A = alkali metals and Tl), which can be regarded as a natural bulk analogue of FeSe monolayers. This compound crystallizes in a tetragonal $ThCr_2Si_2$-type structure composed of alternately stacked FeSe layers and A-ion layers along the *c*-axis (Fig. 1a).[12] This crystal structure intrinsically contains atomically thin FeSe monolayers within a bulk crystal. The FeSe layers in $A_{1-x}Fe_{2-y}Se_2$ possess an identical crystal lattice to that of FeSe, in which Fe atoms form a square lattice and Se atoms occupy apical positions of the edge-shared $FeSe_4$ tetrahedra. The thickness of the FeSe layer in $TlFe_{1.6}Se_2$ is ~3.0 Å, corresponding to a single FeSe slab, which is significantly thinner than the ~1 nm minimum thickness reported for ultrathin FeSe films.[5] Notably, the Fe sites intrinsically contain vacancies (V_{Fe}), forming a $\sqrt{5} \times \sqrt{5} \times 1$ supercell of the $ThCr_2Si_2$-type structure (Fig. 1b). Upon heating, the arrangement of V_{Fe} undergoes a transition between the ordered and disordered states at ~500 K. Theoretical calculations have suggested that the V_{Fe}-ordered $A_{1-x}Fe_{2-y}Se_2$ is a Mott insulator with a Mott gap of ~100 meV,[13,14] and the gap has been experimentally confirmed to be ~430 meV.[15] The V_{Fe}-ordered Mott insulator phase also exhibits long-range antiferromagnetic (AFM) order with a Néel temperature as high as 470–560 K.[12] In contrast, by tuning deficiencies at the A site and the Fe site, $A_{1-x}Fe_{2-y}Se_2$ can exhibit superconductivity with $T_c = 30$ K.[16,17] Note that the electronic transport in $A_{1-x}Fe_{2-y}Se_2$ is mainly governed by FeSe layers, where the electronic states near the Fermi level are dominated by Fe 3d orbitals.[14] As a result, the contribution of A-site ions to the electron transport is relatively limited. Based on these characteristics, $A_{1-x}Fe_{2-y}Se_2$ is expected to exhibit a high PF owing to its two-dimensional FeSe layers naturally embedded within the bulk crystal. In particular, strong electron correlation may lead to an enhanced *S*, while the presence of the ordered and disordered V_{Fe} defects is expected to promote phonon scattering and thereby reduce κ_{lat}.

In this study, we investigate the electronic and phonon transport properties of bulk polycrystalline layered $TlFe_{1.6}Se_2$ as a model system to clarify the effectiveness of embedded two-dimensional FeSe layers in enhancing thermoelectric performance. This compound is much more stable in air than the other $A_{1-x}Fe_{2-y}Se_2$ phases (A = K, Rb, and Cs),[18] and a fully V_{Fe}-ordered phase with high chemical homogeneity can be obtained due to the lower vapor pressure of Tl compared with those of alkali metals.[19] We demonstrate that the PF of $TlFe_{1.6}Se_2$ is significantly higher than bulk FeSe; furthermore, $TlFe_{1.6}Se_2$ exhibits an exceptionally low κ_{lat}, with both the electronic and phonon transport properties strongly modulated by the V_{Fe} ordering and disordering, resulting in an enhanced *ZT*.

2 Synthesis and characterization

2.1 Synthesis

FeSe was synthesized by a solid-state reaction using Fe powder (purity: 99.999%, Kojundo Chemical Lab.) and Se powder (purity: 99.999%, Kojundo Chemical Lab.), mixed at the molar ratio of Fe : Se = 1 : 1. The mixed powders were sealed in an evacuated silica-glass ampule and annealed at 400 °C for 5 h, followed by annealing at 800 °C for 10 h. $TlFe_{1.6}Se_2$ was prepared by a solid-state reaction of fine pieces of the Tl metal (purity: 99.9%, Aldrich) and powders of FeSe and Se. The precursors were mixed in a stoichiometric atomic ratio of Tl : FeSe : Se = 1 : 1.6 : 0.4 and sealed in an Ar-filled stainless-steel tube. The mixture was reacted at 400 °C for 5 h and subsequently at 650 °C for 10 h.[20] The resulting FeSe and $TlFe_{1.6}Se_2$ powders were thoroughly ground and sintered into pellets by a hot-press method at 500 °C for 10 min. All reagents and products were handled in a glove box filled with dry Ar gas (dew point < -80 °C and oxygen concentration < 1 ppm).

2.2 Characterization

Crystalline phases were examined by X-ray diffraction (XRD) in the Bragg–Brentano geometry using a Cu Kα radiation source (MiniFlex600, Rigaku Co.). The lattice parameters were refined by the Pawley method using the TOPAS ver. 4.2 program (Bruker AXS GmbH). The microstructure and chemical compositions (*i.e.*, atomic ratios of Tl, Fe, and Se) of the samples were characterized using an electron probe micro-analyzer (EPMA).

σ and S were simultaneously measured using a ZEM-3 (ULVAC-RIKO, Inc.) under a He atmosphere. S was obtained from the thermoelectric voltage generated under an applied temperature difference (ΔT); the thermoelectromotive force (ΔV) and ΔT were measured simultaneously, and S was determined from the slope of the ΔV–ΔT plots. Pt electrodes deposited by sputtering were used to form ohmic contacts. κ was obtained from $\kappa = D \times C \times d$, where the thermal diffusivity (D) was measured in an Ar atmosphere by the laser flash method (LFA 457, NETZSCH), the specific heat capacity (C) was measured by differential scanning calorimetry (DSC), and the sample density (d) was determined from the mass and geometric dimensions of the pellets. κ_{ele} was calculated using $\kappa_{\mathrm{ele}} = LT\sigma$. L was calculated based on a single-parabolic-band model as follows:[21]

$$L = \left(\frac{k_{\mathrm{B}}}{e}\right)^2 \left(\frac{\left(r+\frac{7}{2}\right)F_{r+5/2}(\eta)}{\left(r+\frac{3}{2}\right)F_{r+\frac{1}{2}}(\eta)} - \left[\frac{\left(r+\frac{5}{2}\right)F_{r+3/2}(\eta)}{\left(r+\frac{3}{2}\right)F_{r+1/2}(\eta)}\right]^2 \right), \quad (1)$$

where k_{B} is the Boltzmann constant. Here, the reduced Fermi energy (η) was obtained based on the free carrier model using the measured S as

$$S = \frac{k_{\mathrm{B}}}{e}\left(\frac{\left(r+\frac{5}{2}\right)F_{r+3/2}(\eta)}{\left(r+\frac{3}{2}\right)F_{r+1/2}(\eta)} - \eta \right) \quad (2)$$

with the Fermi integral defined as

$$F_n(\eta) = \int_0^{\infty} \frac{\chi^n}{1+e^{\chi-\eta}}\mathrm{d}\chi, \quad (3)$$

where $r = -1/2$ is the scattering factor.[22] κ_{lat} was obtained by subtracting κ_{ele} from the total κ, *i.e.*, $\kappa_{\mathrm{lat}} = \kappa - \kappa_{\mathrm{ele}}$. σ and S were measured in the in-plane direction of the hot-pressed pellets, while κ was measured along the out-of-plane direction.

2.3 Theoretical analysis

First-principles calculations were conducted using the projector-augmented wave (PAW) method as implemented in the Vienna *Ab initio* Simulation Package (VASP).[23,24] Tl [5d 6s 6p], Fe [3d 4s], and Se [4s 4p] orbitals were treated as valence states. Variable-cell structural optimizations were performed using the Perdew–Burke–Ernzerhof functional adapted for solids (PBEsol) functional,[25] with a plane-wave cutoff energy of 550 eV, the convergence criteria of 10^{-6} eV for the energy and 0.01 eV Å^{-1} for the force, and a Γ-centered k-mesh with a k-spacing of 0.1 Å^{-1}. Phonon calculations were performed using the ALAMODE codes.[26,27] For FeSe, a 4 × 4 × 2 supercell containing 192 atoms was employed to compute the interatomic force constants (IFCs). For $TlFe_{1.6}Se_2$, a 2 × 2 × 2 supercell with 368 atoms was used to obtain the harmonic IFCs, whereas a 1 × 1 × 1 unit-cell with 46 atoms was used to evaluate the anharmonic IFCs. The harmonic IFCs were fixed to the values determined by the finite-displacement approach,[28,29] and the anharmonic IFCs up to the sixth order were estimated by the compressive sensing lattice dynamics. We included all allowed interactions for the harmonic IFCs, all third-order IFCs within a 12-bohr cutoff radius, and all fourth-to sixth-order IFCs within an 8-bohr cutoff radius. Density functional theory (DFT) calculations to obtain energies and forces were performed using the PBEsol functional with a plane-wave energy cutoff of 400 eV and an energy convergence criterion of 10^{-8} eV. Finite-temperature phonon dispersions were computed by using the self-consistent phonon (SCPH) approach.[30] κ_{lat} was determined by considering the Peierls term, obtained by solving the Peierls–Boltzmann transport equation (PBTE) under the single-mode relaxation time approximation, and the coherent term using the unified formula.[31] The phonon-isotope scatterings were considered.[32] The convergence of κ_{lat} with respect to the q-point mesh was verified using a 7 × 7 × 7 grid for $TlFe_{1.6}Se_2$ and a 15 × 15 × 10 grid for FeSe in the PBTE calculations.

3 Results and discussion

3.1 Electrical transport properties

Crystal structures and microstructure characterizations are summarized in Fig. 2, S1 and S2 in the SI. It was confirmed that $TlFe_{1.6}Se_2$ adopted the V_{Fe}-ordered crystal structure with a space group of *I*4/*m* (Fig. 2a) and FeSe crystallized in a PbO-type α-phase with a space group of *P*4/*nmm* at RT (Fig. S2). Upon heating the $TlFe_{1.6}Se_2$ bulk sample, a transition from the V_{Fe}-ordered structure to the V_{Fe}-disordered structure (space group: *I*4/*mmm*) was observed in the T range of 100 °C–200 °C (Fig. 2b). At higher T, the V_{Fe}-disordered phase became stable.[33] When cooled back to RT, the V_{Fe}-ordered phase reappeared, indicating a reversible structural transition. The relative density of the sintered bulk samples was ∼96%. A minor secondary phase of Fe_7Se_8 (∼2.6 mol%) was detected in the FeSe sample (Fig. S2). Although Fe_7Se_8 is a ferromagnetic metallic phase with a vacancy-ordered NiAs-type crystal structure[34] and may, in principle, contribute to electrical transport, its small fraction

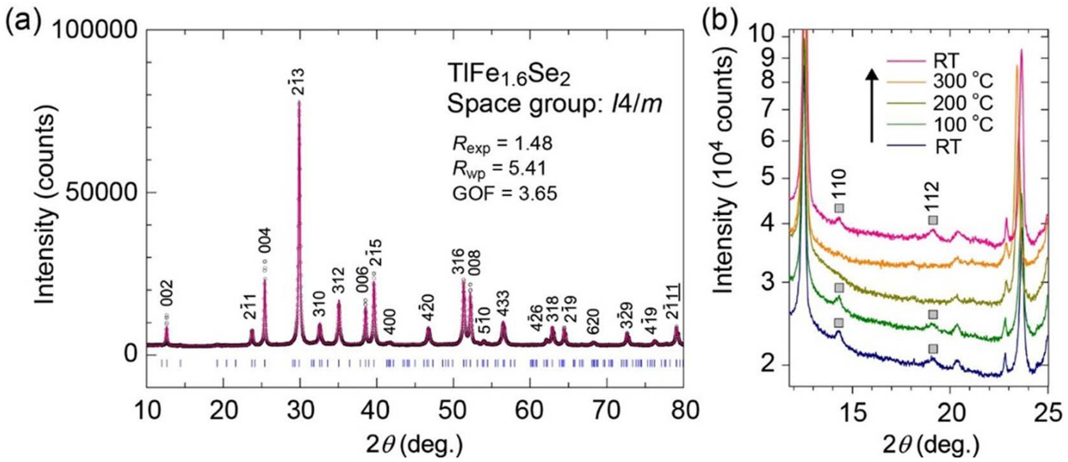

Fig. 2 (a) XRD pattern of the $TlFe_{1.6}Se_2$ bulk sample at RT. (b) Enlarged view of the XRD patterns measured at different T. In the T range from RT to 100 °C, superlattice diffraction peaks of 110 and 112, originating from V_{Fe} ordering, were clearly observed. On the other hand, these peaks disappeared between 200 °C and 300 °C, indicating that V_{Fe} disordering occurred in the T range. Upon cooling back to RT, the superlattice reflections reappeared, demonstrating that the V_{Fe} ordered structure reversibly recovered.

suggests that its influence on the overall transport properties is expected to be limited.

Fig. 3 compares the T dependences of electrical transport properties of $TlFe_{1.6}Se_2$ and FeSe bulk polycrystals. FeSe tends to transform to the NiAs-type β-phase at ~300 °C,[35] and accordingly, all measurements were performed below this temperature to retain the α-phase FeSe. For FeSe, σ exhibited only a slight T dependence; it increased from 1.7×10^5 S cm^{-1} at 50 °C to 1.9×10^5 S cm^{-1} at 290 °C (upper panel of Fig. 3a). At 50 °C, FeSe showed a small positive S of 10 μV K^{-1} (Fig. 3b), which is consistent with the previously reported p-type conduction inferred from Hall-effect measurements.[36] Upon heating, however, the absolute value of S ($|S|$) gradually decreased and the sign eventually became negative around 200 °C, reaching −4 μV K^{-1} at 290 °C. This sign reversal suggests that the dominant carrier type changes with T, which is reasonable given that metallic FeSe is a multiple-band system.[36] In contrast, $TlFe_{1.6}Se_2$ showed a significant increase in σ in the T range of 150 °C–200 °C, rising from 402 S cm^{-1} in the V_{Fe}-ordered phase at 50 °C to 1064 S cm^{-1} at 595 °C upon transition to the V_{Fe}-disordered phase (lower panel of Fig. 3a). Upon cooling, σ reversibly returned to its original value, reflecting the reversibility of the V_{Fe} order–disorder transitions. The sign of S in $TlFe_{1.6}Se_2$ was negative over the entire T range, indicating dominant electron conduction (Fig. 3b). In $TlFe_{1.6}Se_2$, V_{Fe} ordering induces a reconstruction of the electronic structure, associated with antiferromagnetic ordering and the opening of a band gap. The n-type behavior should not be attributed solely to Tl intercalation because the nominal composition is charge-balanced. Rather, it is more likely related to the reconstructed electronic structure associated with V_{Fe} ordering, possibly together with slight off-stoichiometry such as reduced V_{Fe} concentration or Se deficiency. At 50 °C, $TlFe_{1.6}Se_2$ exhibited a large $|S|$ value of 110 μV K^{-1}; however, once the V_{Fe} order was lost through phase transition, $|S|$ decreased substantially around 150 °C and remained almost constant at ~34 μV K^{-1} above 200 °C. This behavior can be attributed to the collapse of the Mott gap upon V_{Fe} disordering, which leads to partial compensation between the electron and hole contributions and consequently reduces the S.

As a reliable Hall voltage could not be obtained by Hall effect measurements, the carrier mobility was estimated as the weighted mobility (μ_w), calculated from σ and S using the following formula:

$$\mu_w = \frac{3h^3\sigma}{8\pi e(2m_e k_B T)^{3/2}}\left[\frac{\exp\left[\frac{|S|}{k_B/e}-2\right]}{1+\exp\left[-5\left(\frac{|S|}{k_B/e}-1\right)\right]} + \frac{\frac{3}{\pi^2}\frac{|S|}{k_B/e}}{1+\exp\left[5\left(\frac{|S|}{k_B/e}-1\right)\right]}\right], \tag{4}$$

where m_e is the free electron mass, k_B is the Boltzmann constant, h is the Planck constant, and e is the elementary charge.[37] The μ_w is related to the drift mobility (μ) through $\mu_w \approx \mu\left(\frac{m^*_{DOS}}{m_e}\right)^{3/2}$, where m^*_{DOS} is the effective mass of the density of state. Using μ_w, the weighted carrier concentration was calculated as $n_w = \frac{\sigma}{e\mu_w}$. In the V_{Fe}-ordered phase, $TlFe_{1.6}Se_2$ exhibited a high μ_w of 60 cm^2 (V^{-1} s^{-1}) at 50 °C, whereas μ_w markedly decreased through transition to the V_{Fe}-disordered phase, reaching 8 cm^2 (V^{-1} s^{-1}) at 595 °C. This reduction is likely associated with enhanced carrier scattering induced by the V_{Fe} disorder. The n_w in the V_{Fe}-ordered phase was ~4.3×10^{19} cm^{-3}, but it increased sharply during the phase-transition and then continued to increase gradually in the V_{Fe}-disordered phase, reaching ~8.0×10^{20} cm^{-3}. This behavior is consistent with the collapse of the Mott gap upon V_{Fe} disordering. These results suggest that both σ and S undergo pronounced changes in response to the transition between the V_{Fe} ordered and

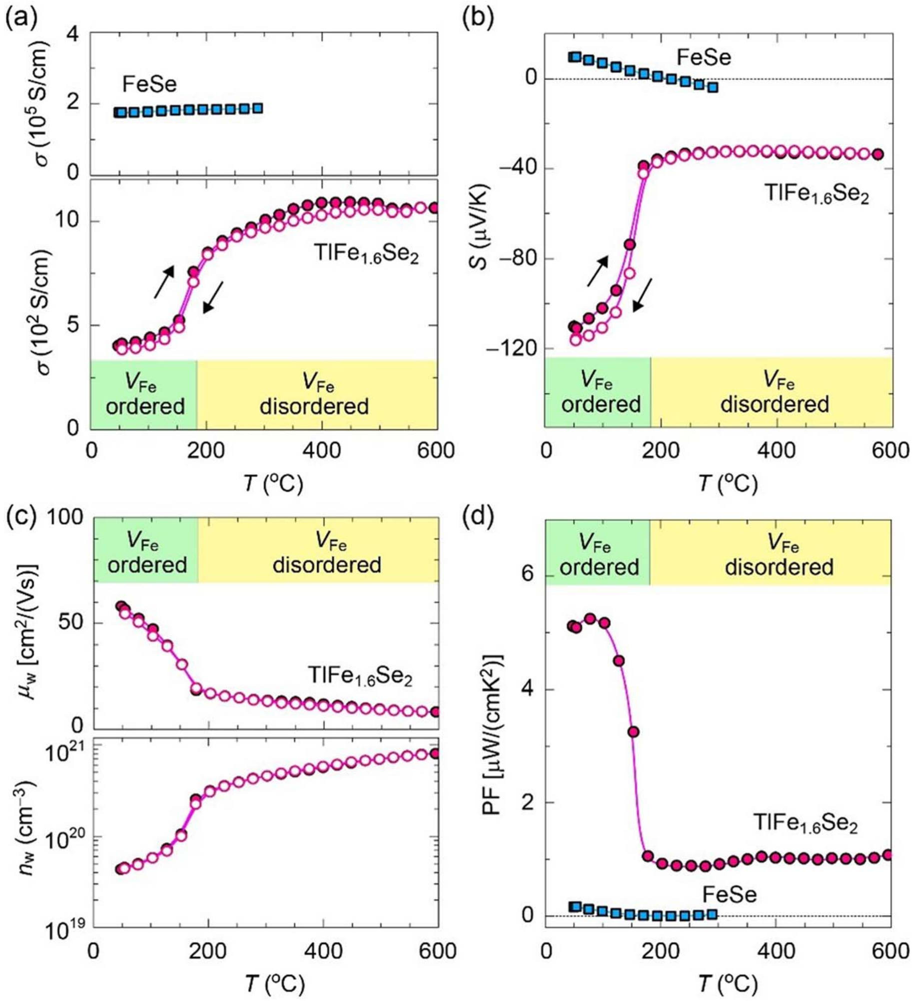

Fig. 3 *T* dependence of the (a) electrical conductivity (*σ*) and (b) Seebeck coefficient (*S*) for the FeSe and $TlFe_{1.6}Se_2$ polycrystals. (c) *T* dependence of the weighted mobility (μ_w) and weighted carrier concentration (n_w) for the $TlFe_{1.6}Se_2$ polycrystal. (d) *T* dependence of the power factor (PF) for the $TlFe_{1.6}Se_2$ and FeSe polycrystals. The green and yellow regions indicate the *T* ranges where the V_{Fe}-ordered and V_{Fe}-disordered phases are stabilized in $TlFe_{1.6}Se_2$, respectively.

disordered states, accompanied by changes in the electronic structure. Fig. 3d summarizes the *T* dependences of PF ($=S^2\sigma$) for $TlFe_{1.6}Se_2$ and FeSe bulk samples. Bulk FeSe exhibited a small *S*, resulting in low PF over the entire *T* range. In contrast, $TlFe_{1.6}Se_2$ showed a pronounced increase in PF in the V_{Fe}-ordered phase, reaching 5.2 μW (cm^{-1} K^{-2}) at 50 °C, which is 30 times higher than that of bulk FeSe. Above 200 °C, where the V_{Fe}-disordered phase was stabilized, PF was reduced to ∼1.0 μW (cm^{-1} K^{-2}). These results demonstrate that $TlFe_{1.6}Se_2$, which contains FeSe monolayers embedded within the bulk crystal, can realize a substantially larger PF than bulk FeSe, with its electrical transport properties strongly modulated by the transition between V_{Fe} ordered and disordered states.

3.2 Thermal and thermoelectric properties

Next, we investigated the thermal transport properties of $TlFe_{1.6}Se_2$ and FeSe polycrystals. The *T* dependences of thermal diffusivity and specific heat capacity are summarized in Fig. S3a and b, SI. Because the specific heat capacity in $TlFe_{1.6}Se_2$ exhibited a peak near the phase-transition temperature (125 °C–200 °C), data in this region were excluded from the analysis of *κ*. Fig. 4a shows the *T* dependence of the total *κ*. FeSe exhibited a *κ* value of 3.2 W (m^{-1} K^{-1}) at 50 °C, which gradually increased with increasing *T* and reached 4.1 W (m^{-1} K^{-1}) at 300 °C. In contrast, $TlFe_{1.6}Se_2$ showed a much lower *κ* of 0.8 W (m^{-1} K^{-1}) at 50 °C, remaining nearly constant up to ∼125 °C. After the transition to the V_{Fe}-disordered phase, *κ* slightly increased to 1.0 W (m^{-1} K^{-1}) and then increased gradually, reaching 1.5 W (m^{-1} K^{-1}) at 500 °C. We next discuss the thermal transport properties by separating electronic and lattice contributions. As shown in Fig. S3c in the SI, κ_{ele} is very large in FeSe than $TlFe_{1.6}Se_2$ due to its higher *σ*, and therefore plays a dominant role in determining *κ*. Fig. 4b compares the *T* dependence of κ_{lat} ($=\kappa - \kappa_{ele}$), in comparison with the typical high-performance thermoelectric materials, including $(Bi_{0.5}Sb_{1.5})Te_3$,[38] $(Pb_{0.98}K_{0.02})(Te_{0.15}Se_{0.85})$,[39] $(Ge_{0.9}In_{0.015}Cu_{0.125})Te$,[40] Cu_2Se,[41] and SnSe[42] polycrystals. FeSe exhibited a κ_{lat} value of 1.8 W (m^{-1}

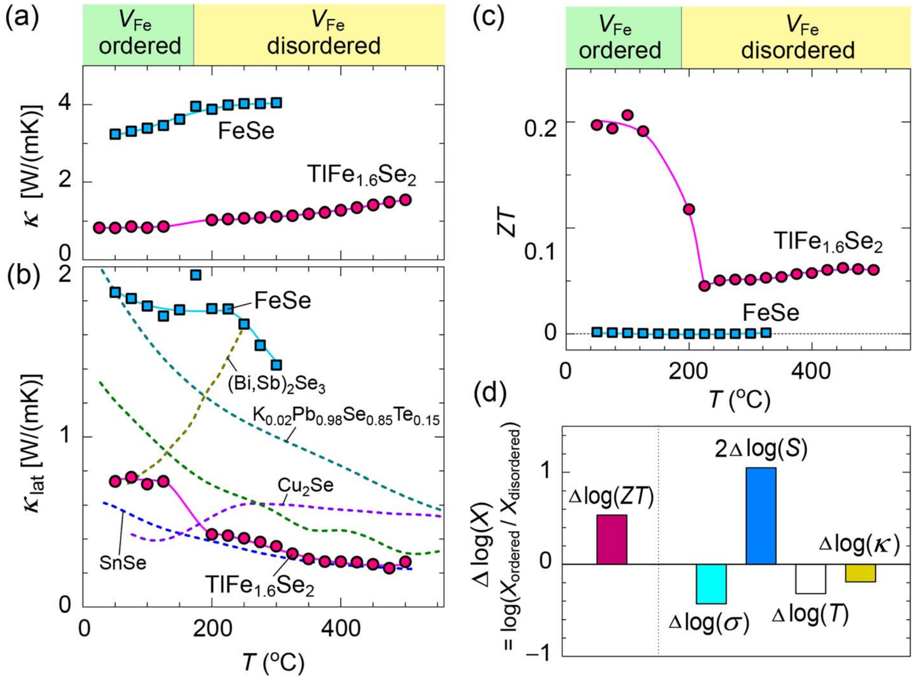

Fig. 4 T dependence of (a) κ and (b) κ_{lat} for the $TlFe_{1.6}Se_2$ and FeSe polycrystals. For comparison, the κ_{lat} *vs.* T curves of typical high-performance thermoelectric materials, including the $(Bi_{0.5}Sb_{1.5})Te_3$,[38] $(Pb_{0.98}K_{0.02})(Te_{0.15}Se_{0.85})$,[39] $(Ge_{0.9}In_{0.015}Cu_{0.125})Te$,[40] Cu_2Se,[41] and SnSe[42] polycrystals, are also shown in (b). (c) T dependence of the dimensionless figure of merit (ZT) for the $TlFe_{1.6}Se_2$ and FeSe polycrystals. (d) Decomposition of contributions in the ZT change across the V_{Fe} order–disorder transition, evaluated between the V_{Fe}-ordered phase at 50 °C and the V_{Fe}-disordered phase at 400 °C. Here, $\Delta\log(X) = \log(X_{ordered}/X_{disordered})$; the positive (negative) values indicate parameters that enhance (reduce) ZT in the V_{Fe}-ordered phase.

K^{-1}) at 50 °C, which gradually decreased with increasing T and reached 1.4 W (m^{-1} K^{-1}) at 300 °C. In contrast, $TlFe_{1.6}Se_2$ showed an extremely low κ_{lat} of 0.7 W (m^{-1} K^{-1}) at 50 °C in the V_{Fe}-ordered phase, where κ_{lat} exhibited a weak T dependence and remained nearly constant. After the transition to the V_{Fe}-disordered phase, κ_{lat} decreased further to 0.4 W (m^{-1} K^{-1}) at 200 °C and ∼0.2 W (m^{-1} K^{-1}) at 500 °C. In addition, these values are lower than those of high-performance thermoelectric materials with intrinsically low κ_{lat}, and are comparable to the lowest κ_{lat} values reported for layered SnSe polycrystals.[42] Therefore, $TlFe_{1.6}Se_2$, containing FeSe layers with V_{Fe} order–disorder structures, is demonstrated to achieve extremely low κ_{lat}.

Here, the Lorenz number (L) for κ_{ele} was estimated using a single-parabolic-band model with a scattering parameter of $r = -1/2$. Since $TlFe_{1.6}Se_2$ is a multiband Mott system with strong electron correlations, L depends on the Fermi level, effective mass and r, which are difficult to determine uniquely because of the complex electronic structure and the uncertainty in the dominant scattering mechanism. Then, we evaluated L over a broad physically reasonable range of r (−1/2 to 2) and Fermi level. For the V_{Fe}-ordered phase ($n = 4.2 \times 10^{19}$ cm^{-3}), L varies within 1.5–2.8 × 10^{-8} WΩ K^{-2}, corresponding to an uncertainty of ±30–40%. This leads to a variation of κ_{ele} from 0.05 to 0.11 W (m^{-1} K^{-1}) (nominal value: 0.084 W (m^{-1} K^{-1})), resulting in κ_{lat} ranging from 0.71 to 0.79 W (m^{-1} K^{-1}) (nominal value: 0.74 W (m^{-1} K^{-1})), indicating a relatively limited uncertainty. In contrast, for the V_{Fe}-disordered phase with a higher carrier concentration ($n = 6.0 \times 10^{20}$ cm^{-3}), L becomes much less sensitive to model parameters and converges to a narrow range of 2.4–2.5 × 10^{-8} WΩ K^{-2}, close to the degenerate limit. In this case, κ_{ele} is ∼1.01 W (m^{-1} K^{-1}), with a variation of less than ±0.05 W (m^{-1} K^{-1}), leading to only minor alternations in κ_{lat} (∼0.27 W (m^{-1} K^{-1})). Although the exact value of L depends on the model assumptions, the resulting uncertainty in κ_{lat} remains limited. Therefore, even when this uncertainty is taken into account, $TlFe_{1.6}Se_2$ exhibits intrinsically low κ_{lat}.

Based on the electronic and thermal transport properties discussed above, we evaluated the overall thermoelectric performance of $TlFe_{1.6}Se_2$ and FeSe (Fig. 4b). Bulk FeSe exhibited both a small S and a high κ, resulting in low ZT over the entire T range, consistent with its metallic electronic structure. In contrast, $TlFe_{1.6}Se_2$ showed a pronounced increase of ZT in the V_{Fe}-ordered phase, reaching ∼0.2 at 50 °C, which is two orders of magnitude higher than that of bulk FeSe, whereas ZT was limited to ∼0.05 in the V_{Fe}-disordered phase at $T > 200$ °C. To clarify the origin of this strong contrast in ZT between the V_{Fe}-ordered and V_{Fe}-disordered phases, the relative change in ZT across the transition was analyzed by decomposing ZT into contributions from individual transport parameters. Taking the logarithm of $ZT = S^2\sigma T/\kappa$, we obtain $\Delta\log(ZT) = \Delta\log(\sigma) + 2\Delta\log(S) + \Delta\log(T) - \Delta\log(\kappa)$, which are the approximations of relative differences, $\frac{\Delta ZT}{ZT} \approx \frac{\Delta\sigma}{\sigma} + \frac{2\Delta S}{S} + \frac{\Delta T}{T} - \frac{\Delta\kappa}{\kappa}$. Here, the contributions are evaluated using logarithmic differences, defined as $\Delta\log(X) = \log(X_{\text{ordered}}) - \log(X_{\text{disordered}})$, which represents the change in each parameter across the transition. Fig. 4c summarizes the changes in each transport parameter between the V_{Fe}-ordered phase at 50 °C and the V_{Fe}-disordered phase at 400 °C. These temperatures were chosen because they lie sufficiently far from the order–disorder transition, ensuring high phase purity in the fully V_{Fe}-ordered and fully V_{Fe}-disordered states, respectively. This allows us to compare the intrinsic transport properties of the pure phases. Positive values indicate quantities that are enhanced in the V_{Fe}-ordered phase and therefore contribute positively to the increase in *ZT*, whereas negative values indicate factors that reduce *ZT*. Note that κ appears in the dominator of *ZT*, an increase of κ (*i.e.*, positive $\Delta\log(\kappa)$) contributes negatively to *ZT*. Although κ_{lat} is effectively reduced in the V_{Fe}-disordered phase, the overall contribution of the total κ to *ZT* is only slightly negative. This is because the transition to a metallic state simultaneously leads to a substantial increase in κ_{ele}, which compensates for the benefit of the reduced κ_{lat}. In contrast, *S* exhibits the largest positive contribution, indicating that the enhancement of *ZT* in the V_{Fe}-ordered phase is predominantly driven by the large *S* associated with the opening of the Mott gap. To assess possible effects arising from the large temperature difference in the above comparison, the *ZT* decomposition analysis was also performed with a closer temperature difference of 125 °C for the ordered phase and 225 °C for the disordered phase (Fig. S4). The results confirm that the overall conclusion remains unchanged; the dominant contribution to the *ZT* enhancement arises from the increase in *S*. These results demonstrate that V_{Fe} ordering in layered $\text{TlFe}_{1.6}\text{Se}_2$ enables a favorable balance between electronic and thermal transport, allowing relatively large PF and *ZT* values to be realized in the bulk form.

To further elucidate the underlying mechanism responsible for the low κ_{lat} in $\text{TlFe}_{1.6}\text{Se}_2$, we conducted first-principles anharmonic lattice dynamics (ALD) calculations, as implemented in the ALAMODE code.[26,27] We first calculated the harmonic phonon dispersion of $\text{TlFe}_{1.6}\text{Se}_2$, shown as the dotted black lines in Fig. 5a. Imaginary modes appear at the *X* and *R* points, indicating that the structure is dynamically unstable at $T = 0$ K within the harmonic approximation. To account for the temperature effect, SCPH calculations were performed. At $T = 300$ K, as shown by the solid blue lines in Fig. 5a, all phonon frequencies become positive, meaning that the previously imaginary modes are stabilized after including the temperature-induced anharmonic correction. $\text{TlFe}_{1.6}\text{Se}_2$ exhibits a large number of phonon branches with strong mode entanglement (left panel of Fig. 5a). The acoustic phonons and the low-frequency optical phonons up to ~2.5 THz exhibit relatively flat dispersions, indicating low phonon group velocities and the suppression of heat transport. The partial phonon density of states (DOSs) projected on each element for the V_{Fe}-ordered $\text{TlFe}_{1.6}\text{Se}_2$ at $T = 300$ K is shown in the right panel of Fig. 5a. The phonon DOS reveals that vibrations of the heavy Tl atoms predominantly contribute to the low-frequency phonon modes below ~2 THz. These Tl-derived optical modes exhibit extremely flat dispersions and strongly overlap with the acoustic branches, indicating highly localized vibrations associated with weak coupling between the Tl atoms and the Fe–Se framework. In contrast, the higher-frequency phonon branches are mainly associated with vibrations of Fe and Se atoms. For comparison, the phonon dispersion and partial phonon DOS of FeSe at $T = 300$ K are shown in Fig. 5b. FeSe exhibits a much simpler phonon spectrum with fewer but strongly dispersive branches (left panel of Fig. 5b), consistent with its relatively simple crystal structure. While the phonon dispersions along the out-of-plane *Γ*–*Z* direction are relatively weak, much stronger dispersions are observed along the in-plane *Γ*–*X* and *Γ*–*M* direction, extending up to ~5 THz. The broad frequency distribution of the Fe–Se vibrational modes in the partial phonon DOSs (right panel of Fig. 5b) reflects the strong Fe–Se bonding and is consistent with the highly dispersive phonon branches. Compared with bulk FeSe, the Fe–Se phonon branches in $\text{TlFe}_{1.6}\text{Se}_2$ exhibit reduced dispersion and stronger mode entanglement, reflecting the reduced symmetry and structural complexity of FeSe layers caused by V_{Fe} and interlayer Tl atoms.

We subsequently calculated κ_{lat} by solving the Peierls–Boltzmann transport equation (PBTE) within the relaxation time approximation. Fig. 5c and d present the anisotropic κ_{lat} components along the in-plane (*xx* and *yy*) and the out-of-plane (*zz*) directions for $\text{TlFe}_{1.6}\text{Se}_2$ and FeSe as a function of *T*, considering the contribution from the coherent term. The effect of the coherent contribution on the *T* dependence of κ_{lat} is shown in Fig. S5 in the SI. κ_{lat} for $\text{TlFe}_{1.6}\text{Se}_2$ was calculated based on the ordered structure and is therefore shown only at low temperatures. In layered FeSe, the pronounced structural anisotropy leads to a strong crystallographic-direction dependence of κ_{lat} (Fig. 5d). At 27 °C, the in-plane $\kappa_{\text{lat\_}xx}$ ($\kappa_{\text{lat\_}yy}$) reaches an exceptionally high value of 33.74 W (m^{-1} K^{-1}) within the FeSe layers, whereas $\kappa_{\text{lat\_}zz}$ is only 1.09 W (m^{-1} K^{-1}), resulting in an extremely large anisotropy ratio of ~33. In contrast, $\text{TlFe}_{1.6}\text{Se}_2$ exhibits intrinsically suppressed κ_{lat} even along the in-plane direction (Fig. 5c). At 27 °C, $\kappa_{\text{lat\_}xx}$ ($\kappa_{\text{lat\_}yy}$) is only 1.43 W (m^{-1} K^{-1}), more than an order of magnitude lower than that of FeSe, while $\kappa_{\text{lat\_}zz}$ is further reduced to 0.42 W (m^{-1} K^{-1}).

To facilitate comparison with the experimental data for anisotropic polycrystalline materials, we evaluated orientation-averaged κ_{lat} values using both a harmonic-mean (series-type) average, $\kappa_{\text{lat}}^{\text{series}} = \left(\frac{1}{\kappa_{xx}} + \frac{1}{\kappa_{yy}} + \frac{1}{\kappa_{zz}}\right)^{-1} \times 3$, and an arithmetic-mean (parallel-type) average, $\kappa_{\text{lat}}^{\text{parallel}} = \frac{\kappa_{xx} + \kappa_{yy} + \kappa_{zz}}{3}$, which are plotted together with the measured κ_{lat} of V_{Fe}-ordered $\text{TlFe}_{1.6}\text{Se}_2$ and FeSe polycrystals (Fig. 5c and d). The parallel-type average corresponds to a transport regime in which heat flows independently along different crystallographic directions, whereas the series-type average represents a transport regime largely controlled by the lowest κ_{lat} component. Both $\text{TlFe}_{1.6}\text{Se}_2$ and FeSe polycrystals exhibit κ_{lat} close to $\kappa_{\text{lat}}^{\text{series}}$, indicating that heat transport in the polycrystalline form is largely governed by the low out-of-plane component. In FeSe, the intrinsically high in-plane κ_{lat} is strongly suppressed in the polycrystal, whereas in

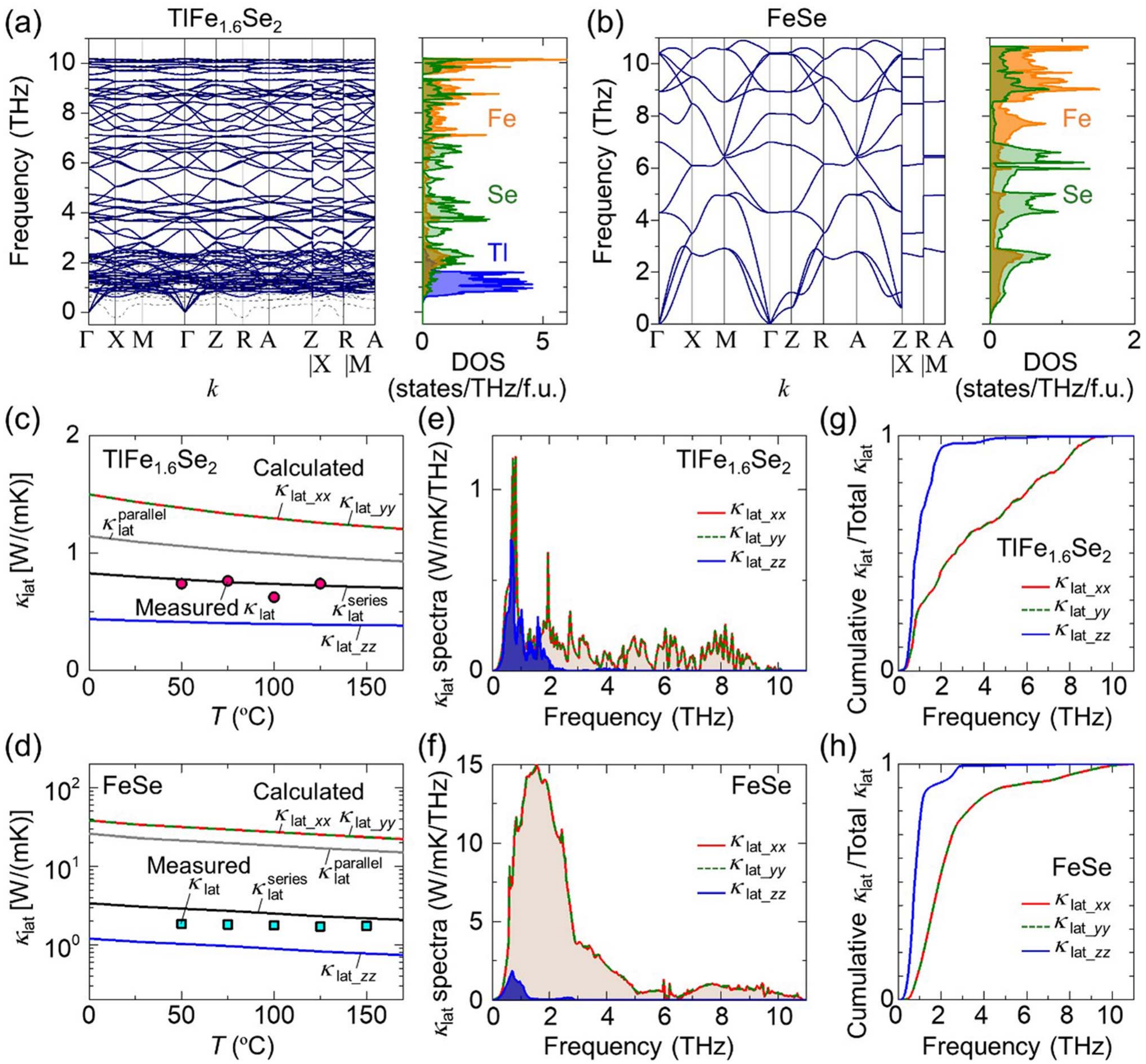

Fig. 5 Anharmonic phonon dispersions (left panels) and partial phonon density of states (DOS) projected on each element (right panels) for (a) $\mathrm{TlFe_{1.6}Se_2}$ and (b) FeSe at $T = 300$ K. The dotted black lines in (a) represent the phonon dispersion calculated within the harmonic approximation. The k-path is Γ (0.0, 0.0, 0.0), X (0.0, 0.5, 0.0), M (0.5, 0.5, 0.0), Z (0.0, 0.0, 0.5), R (0.0, 0.5, 0.5), and A (0.5, 0.5, 0.5). T dependence of the calculated κ_{lat} along the xx and yy (parallel to FeSe layer) and zz (perpendicular to FeSe layer) axes for (c) $\mathrm{TlFe_{1.6}Se_2}$ and (d) FeSe. The averaged κ_{lat} values obtained using the series $\left(\kappa_{\mathrm{lat}}^{\mathrm{series}} = \left(\frac{1}{\kappa_{xx}} + \frac{1}{\kappa_{yy}} + \frac{1}{\kappa_{zz}}\right)^{-1} \times 3\right)$ and parallel $\left(\kappa_{\mathrm{lat}}^{\mathrm{parallel}} = \frac{\kappa_{xx} + \kappa_{yy} + \kappa_{zz}}{3}\right)$ conduction models are also shown. The experimentally measured κ_{lat} for the V_{Fe}-ordered $\mathrm{TlFe_{1.6}Se_2}$ and FeSe polycrystals are also plotted for comparison. Comparison of the κ_{lat} spectra for (e) $\mathrm{TlFe_{1.6}Se_2}$ and (f) FeSe at $T = 300$ K. Frequency-dependent cumulative κ_{lat} for (g) $\mathrm{TlFe_{1.6}Se_2}$ and (h) FeSe at $T = 300$ K.

$\mathrm{TlFe_{1.6}Se_2}$, the already low in-plane κ_{lat} is further reduced by the out-of-plane contribution.

Fig. 5e and f compare the anisotropic frequency-resolved κ_{lat} at $T = 300$ K for $\mathrm{TlFe_{1.6}Se_2}$ and FeSe, while the frequency-dependent cumulative κ_{lat} are shown in Fig. 5g and h. In FeSe, the in-plane $\kappa_{\mathrm{lat\_}xx}$ ($\kappa_{\mathrm{lat\_}yy}$) exhibits a pronounced peak around ~1.5 THz, whereas the out-of-plane $\kappa_{\mathrm{lat\_}zz}$ shows a small peak at ~0.5 THz (Fig. 5f). As shown in Fig. 5h, phonons below ~5 THz account for about 90% of the total $\kappa_{\mathrm{lat\_}xx}$ ($\kappa_{\mathrm{lat\_}yy}$), indicating that heat transport is dominated by acoustic phonon modes. The contribution to $\kappa_{\mathrm{lat\_}zz}$ is confined to frequencies below ~1.5 THz and arises almost exclusively from acoustic phonons, reflecting the intrinsically inefficient thermal transport along the out-of-plane direction. This anisotropic behavior is consistent with the steep phonon branches along the Γ–X and Γ–M directions, arising from highly dispersive in-plane acoustic phonons of the Fe–Se framework, and the much less dispersive phonon branches along the Γ–Z direction, reflecting the layered structural characteristic (Fig. 5b).

For $TlFe_{1.6}Se_2$, the frequency-resolved κ_{lat} shows a clear directional contrast (Fig. 5e). The in-plane κ_{lat_xx} (κ_{lat_yy}) spans a much broader frequency range extending up to ~10 THz, mainly associated with the vibration of the Fe–Se framework (left panel of Fig. 5a). In contrast, the out-of-plane κ_{lat_zz} is dominated by phonons below ~2 THz, primarily arising from the vibrations of the heavy Tl atoms (right panel of Fig. 5a). The cumulative κ_{lat} (Fig. 5g) further clarifies this difference. Below 2.5 THz, only ~49% of κ_{lat_xx} (κ_{lat_yy}) is accumulated, whereas more than ~96% of κ_{lat_zz} is contributed within this range. This indicates that higher-frequency optical modes contribute to more than half of the in-plane heat transport in $TlFe_{1.6}Se_2$. Such behavior is markedly different from that of FeSe, where the in-plane heat transport is dominated almost entirely by low-frequency phonons. Consequently, the contribution of low-frequency phonons to κ_{lat_xx} (κ_{lat_yy}) is strongly suppressed in $TlFe_{1.6}Se_2$.

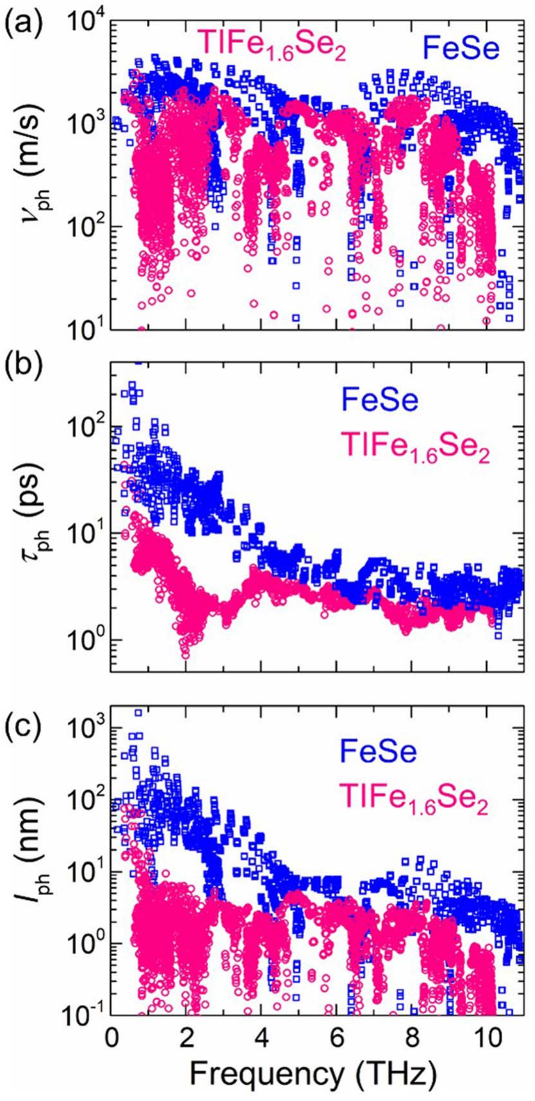

Fig. 6 (a) Phonon group velocity (ν_{ph}), (b) phonon lifetime (τ_{ph}), and (c) phonon mean free path (l_{ph}) in terms of the phonon frequency for $TlFe_{1.6}Se_2$ (pink plots) and FeSe (blue plots) at $T = 300$ K.

Fig. 6 compares the phonon group velocity (ν_{ph}), phonon lifetime (τ_{ph}), and phonon mean free path (l_{ph}) as functions of phonon frequency. $TlFe_{1.6}Se_2$ exhibits much lower ν_{ph} than FeSe over a wide frequency range (Fig. 6a), reflecting the flatter acoustic and optical phonon branches shown in Fig. 5a. This reduction in ν_{ph} originates from the weak coupling between the heavy Tl atoms and the Fe–Se framework, which effectively softens the lattice vibrations and limits phonon propagation. More importantly, τ_{ph} in $TlFe_{1.6}Se_2$ is reduced over a broad frequency range, with an exceptionally strong suppression observed for phonons below ~4 THz (Fig. 6b). In the lowest-frequency region below ~1.5 THz, this reduction is primarily associated with Tl-related vibrational modes, whereas in the higher-frequency region up to ~4 THz, it mainly affects phonons derived from the Fe–Se framework. As a result, l_{ph} in $TlFe_{1.6}Se_2$ is strongly suppressed, particularly because the τ_{ph} of phonon modes below ~4 THz become extremely short (Fig. 6c). These results indicate that two distinct scattering mechanisms operate in different frequency regimes: low-frequency phonon scattering induced by the weakly bound heavy Tl atoms, and the additional scattering of the Fe–Se framework phonons in $TlFe_{1.6}Se_2$.

To further clarify the microscopic origin of the enhanced phonon scattering in the Fe–Se framework, we evaluated the Fe–Se bonding characteristics in $TlFe_{1.6}Se_2$ and FeSe by estimating their bonding energies using crystal orbital Hamilton population (COHP)[43] analysis, as implemented in the LOBSTER code.[44] The –iCOHP values, obtained by integrating –COHP up to the Fermi level and corresponding to the bond strength, are 2.35 eV per bond for the Fe–Se bonds in FeSe and range from 2.17 to 2.51 eV per bond in $TlFe_{1.6}Se_2$, with an average value of 2.34 eV per bond. The Fe–Se bond length in FeSe is 2.278 Å, while that in $TlFe_{1.6}Se_2$ spans a range of 2.242–2.290 Å, yielding an average bond length of 2.272 Å (Fig. S6 in SI). These results indicate that the average Fe–Se bond strength and bond length are nearly identical in $TlFe_{1.6}Se_2$ and FeSe. In contrast, $TlFe_{1.6}Se_2$ exhibits a pronounced distribution of Fe–Se bond strengths, reflecting bond heterogeneity induced by V_{Fe} ordering. Such bond heterogeneity provides an additional phonon-scattering channel, particularly for intermediate- and high-frequency Fe–Se vibrational modes, and plays a key role in shortening τ_{ph} and suppressing κ_{lat}. This is further supported by the interatomic force constant (IFC) distributions (Fig. S7 in SI), showing the broadened force-constant distribution in $TlFe_{1.6}Se_2$ compared to FeSe. In addition, the three-phonon scattering phase space (SPS) is significantly enhanced, particularly in the 1.5–4 THz region (Fig. S8 in SI), indicating an increased number of scattering channels in this frequency range. This frequency range is dominated by the Fe–Se vibrational modes with strong acoustic–optical mixing (Fig. 5a), making them sensitive, especially to the bond heterogeneity. The dominance of force-constant disorder is also inferred from the frequency-selective reduction of phonon lifetimes between 1.5 and 4 THz (Fig. 6b). Therefore, the lifetime reduction in this frequency window is primarily driven by emission channels activated by the force-constant disorder, while mass disorder provides a secondary background contribution. Such bond-heterogeneity-induced phonon scattering has also been reported in a variety of complex crystalline materials, where local fluctuations in bonding strength or force constants give rise to enhanced anharmonic phonon scattering and reduced κ_{lat}.[45–49] In the V_{Fe}-disordered phase, this bond heterogeneity is further amplified by the random distribution of V_{Fe}, introducing additional mass and force-constant disorder. This disorder-driven enhancement of phonon scattering accounts for the further reduction of κ_{lat} observed experimentally at elevated temperatures. Direct first-principles calculations for the V_{Fe} disordered phases were not performed due to the large configurational space associated with random vacancy distributions and the limitation of our computational resources. Random V_{Fe} distributions are expected to introduce spatially uncorrelated force-constant disorder, which is likely more effective in scattering phonons than the ordered structure, leading to additional suppression of κ_{lat}.

4 Conclusions

We investigated the thermoelectric properties of layered $\text{TlFe}_{1.6}\text{Se}_2$, motivated by the expectation that its embedded two-dimensional FeSe transport layers, together with the V_{Fe} order–disorder transition, could provide a unique combination of enhanced PF and suppressed κ_{lat}. $\text{TlFe}_{1.6}\text{Se}_2$ exhibited an exceptionally low κ_{lat}, reaching ~0.7 W (m^{-1} K^{-1}) in the V_{Fe}-ordered phase at 50 °C and further decreasing to ~0.2 W (m^{-1} K^{-1}) in the V_{Fe}-disordered phase at 500 °C, which is comparable to or even lower than those of high-performance thermoelectric materials with intrinsically low κ_{lat}. Notably, unlike layered FeSe, which shows extremely high in-plane κ_{lat} and strong anisotropy, κ_{lat} in $\text{TlFe}_{1.6}\text{Se}_2$ is intrinsically suppressed even along the in-plane direction. This ultralow κ_{lat} originates from the combined effects of weakly bound heavy Tl atoms, which reduce phonon group velocities, and enhanced phonon scattering caused by the V_{Fe}-induced bond heterogeneity within the Fe–Se framework.

The electronic transport properties are strongly modulated across the transition between the V_{Fe} ordered and disordered states. In the V_{Fe}-disordered phase, $\text{TlFe}_{1.6}\text{Se}_2$ exhibits a metallic state with enhanced σ and ultralow κ_{lat}; however, strong carrier compensation significantly reduces S, limiting the ZT value to ~0.05. In contrast, in the V_{Fe}-ordered phase, the opening of a Mott gap leads to a large S of ~110 μV K^{-1} at 50 °C, resulting in an enhanced PF of 5.2 μW (cm^{-1} K^{-2}) and a ZT of ~0.2. These results demonstrate that the confinement of FeSe layers within bulk $\text{TlFe}_{1.6}\text{Se}_2$ enables a substantial PF enhancement compared with bulk FeSe, while V_{Fe} ordering and disordering play complementary roles by tuning carrier transport and strongly suppressing κ_{lat}. Looking forward, further enhancement of ZT may be achieved by optimizing carrier concentration in the V_{Fe}-ordered phase and by tuning the V_{Fe} concentration.

Although the incorporation of two-dimensional FeSe layers suggested the possibility of achieving a high PF comparable to that of FeSe monolayers, the obtained PF is substantially lower. This difference is primarily attributed to the much lower carrier mobility in $\text{TlFe}_{1.6}\text{Se}_2$, which is about four orders of magnitude smaller than that of FeSe monolayers, likely due to the polycrystalline nature and enhanced carrier scattering arising from V_{Fe} ordering/disordering and interactions involving Tl atoms. In contrast, the exceptionally high mobility in FeSe monolayers is realized for in-plane transport in the two-dimensional electronic structure. To clarify the intrinsic transport properties and to potentially realize higher PF in $\text{TlFe}_{1.6}\text{Se}_2$, studies using single crystals or epitaxial thin films will be essential, as they enable selective probing of in-plane transport in the embedded FeSe layers.

Extending this concept to other alkali-based $\text{A}_{1-x}\text{Fe}_{2-y}\text{Se}_2$ (A = K, Rb, and Cs) is an attractive direction, as they consist of FeSe layers with V_{Fe}, forming quasi-two-dimensional frameworks, and exhibit high electrical conductivity. Moreover, these systems show high-T_{c} superconductivity, reminiscent of FeSe monolayers, suggesting a close connection between their electronic structures. In addition, the V_{Fe} concentration in these systems can be tuned over a wide range,[16,17] providing a versatile platform for controlling carrier concentration and optimizing thermoelectric performance. However, their poor air stability, precise control of vacancy ordering, and suppression of phase separation remain significant challenges.[15] The growth of high-quality single crystals or epitaxial thin films will also be essential to clarify the intrinsic transport properties. A possible strategy to address air stability is partial substitution or solid-solution formation with air-stable Tl-based compounds,[50] which may enable simultaneous control of environmental stability and thermoelectric performance.

Taken together, the present study highlights the confinement of two-dimensional FeSe layers, combined with vacancy-order control, as a promising design strategy for bulk thermoelectric materials that combine large PF with intrinsically low κ_{lat}.

Conflicts of interest

There are no conflicts to declare.

Data availability

The data supporting this study are included within the article and its supplementary information (SI). Supplementary information: the SI includes the bulk synthesis, characterization, and theoretical calculations for $\text{TlFe}_{1.6}\text{Se}_2$ and FeSe. See DOI: https://doi.org/10.1039/d6ta02075e.

Acknowledgements

This work was supported by the MEXT Program: Data Creation and Utilization Type Material Research and Development Project (Grant No. JPMXP1122683430), the Design and Engineering by Joint Inverse Innovation for Materials Architecture, and also by a project of Kanagawa Institute of Industrial Science and Technology (KISTEC). X. He was supported by Japan Society for the Promotion of Science (JSPS) through the Grant-in-Aid for Research Activity Start-up (Grant No. 25K23539). T. Katase was supported by the Special Award for Science Tokyo Advanced

Researchers (STAR) funded by the Institute of Science Tokyo and JSPS through the Grant-in-Aids for Scientific Research (B) (Grant No. 26K01206), Scientific Research (A) (Grant No. 24H00314), Scientific Research (S) (Grant No. 22H04964), and Challenging Research (Exploratory) (Grant No. 24K21671). H. Hi. was supported by JSPS through the Grants-in-Aid for Scientific Research (A) (Grant No. JP20H00302, JP21H04612, and JP24H00376). The numerical calculations were carried out on the TSUBAME4.0 supercomputer at the Institute of Science Tokyo supported by the MEXT Project of the Tokyo Tech Academy for Convergence of Materials and Informatics (TAC-MI), and the supercomputer at the Research Center for Computational Science, Okazaki, Japan. The crystal structures in Fig. 1 were drawn using the VESTA code.[51]

References

1 F. J. DiSalvo, *Science*, 1999, **285**, 703–706.
2 L. E. Bell, *Science*, 2008, **321**, 1457–1461.
3 Q. H. Zhang, X. Y. Huang, S. Q. Bai, X. Shi, C. Uher and L. D. Chen, *Adv. Eng. Mater.*, 2016, **18**, 194–213.
4 G. J. Snyder and E. S. Toberer, *Nat. Mater.*, 2008, **7**, 105–114.
5 S. Shimizu, J. Shiogai, N. Takemori, S. Sakai, H. Ikeda, R. Arita, T. Nojima, A. Tsukazaki and Y. Iwasa, *Nat. Commun.*, 2019, **10**, 825.
6 F.-C. Hsu, J.-Y. Luo, K.-W. Yeh, T.-K. Chen, T.-W. Huang, P. M. Wu, Y.-C. Lee, Y.-L. Huang, Y.-Y. Chu, D.-C. Yan and M.-K. Wu, *Proc. Natl. Acad. Sci. U. S. A.*, 2008, **105**, 14262–14264.
7 J.-F. Ge, Z.-L. Liu, C. Liu, C.-L. Gao, D. Qian, Q.-K. Xue, Y. Liu and J.-F. Jia, *Nat. Mater.*, 2014, **14**, 285–289.
8 Y. Machida, K. Tomokuni, T. Isono, Y. Nakajima and T. Tamegai, *J. Phys. Soc. Jpn.*, 2009, **78**, 073705.
9 J. G. Checkelsky, R. Thomale, L. Li, G. F. Chen, J. L. Luo, N. L. Wang and N. P. Ong, *Phys. Rev. B:Condens. Matter Mater. Phys.*, 2012, **86**, 180502(R).
10 P. Devi Lodhi, N. Kaurav, K. K. Choudhary and Y. K. Kuo, *J. Low Temp. Phys.*, 2019, **196**, 494–509.
11 C. B. Satterthwaite and R. W. Ure, *Phys. Rev.*, 1957, **108**, 1164–1170.
12 F. Ye, S. Chi, W. Bao, X. F. Wang, J. J. Ying, X. H. Chen, H. D. Wang, C. H. Dong and M. Fang, *Phys. Rev. Lett.*, 2011, **107**, 137003.
13 R. Yu, J.-X. Zhu and Q. Si, *Phys. Rev. Lett.*, 2011, **106**, 186401.
14 X.-W. Yan, M. Gao, Z.-Y. Lu and T. Xiang, *Phys. Rev. Lett.*, 2011, **106**, 087005.
15 W. Li, H. Ding, P. Deng, K. Chang, C. Song, K. He, L. Wang, X. Ma, J.-P. Hu, X. Chen and Q.-K. Xue, *Nat. Phys.*, 2012, **8**, 126–130.
16 J. Guo, S. Jin, G. Wang, S. Wang, K. Zhu, T. Zhou, M. He and X. Chen, *Phys. Rev. B:Condens. Matter Mater. Phys.*, 2010, **82**, 180520.
17 Y. J. Yan, M. Zhang, A. F. Wang, J. J. Ying, Z. Y. Li, W. Qin, X. G. Luo, J. Q. Li, J. Hu and X. H. Chen, *Sci. Rep.*, 2012, **2**, 212.
18 B. C. Sales, M. A. McGuire, A. F. May, H. Cao, B. C. Chakoumakos and A. S. Sefat, *Phys. Rev. B:Condens. Matter Mater. Phys.*, 2011, **83**, 224510.
19 A. F. May, M. A. McGuire, H. Cao, I. Sergueev, C. Cantoni, B. C. Chakoumakos, D. S. Parker and B. C. Sales, *Phys. Rev. Lett.*, 2012, **109**, 077003.
20 T. Katase, H. Hiramatsu, T. Kamiya and H. Hosono, *Proc. Natl. Acad. Sci.*, 2014, **111**, 3979–3983.
21 H. J. Goldsmid, *Introduction to Thermoelectricity*, Springer, Heidelberg, 2009.
22 X. He, S. Kimura, T. Katase, T. Tadano, S. Matsuishi, M. Minohara, H. Hiramatsu, H. Kumigashira, H. Hosono and T. Kamiya, *Adv. Sci.*, 2023, **11**, 2307058.
23 G. Kresse and D. Joubert, *Phys. Rev. B:Condens. Matter Mater. Phys.*, 1999, **59**, 1758–1775.
24 G. Kresse and J. Furthmüller, *Phys. Rev. B:Condens. Matter Mater. Phys.*, 1996, **54**, 11169–11186.
25 J. P. Perdew, A. Ruzsinszky, G. I. Csonka, O. A. Vydrov, G. E. Scuseria, L. A. Constantin, X. Zhou and K. Burke, *Phys. Rev. Lett.*, 2008, **100**, 136406.
26 T. Tadano and S. Tsuneyuki, *Phys. Rev. B:Condens. Matter Mater. Phys.*, 2015, **92**, 054301.
27 T. Tadano, Y. Gohda and S. Tsuneyuki, *J. Phys.: Condens. Matter*, 2014, **26**, 225402.
28 G. Kresse, J. Furthmüller and J. Hafner, *Europhys. Lett.*, 1995, **32**, 729–734.
29 K. Parlinski, Z. Li and Y. Kawazoe, *Phys. Rev. Lett.*, 1997, **78**, 4063–4066.
30 T. Tadano and S. Tsuneyuki, *Phys. Rev. B:Condens. Matter Mater. Phys.*, 2015, **92**, 054301.
31 M. Simoncelli, N. Marzari and F. Mauri, *Nat. Phys.*, 2019, **15**, 809–813.
32 S. Tamura, *Phys. Rev. B:Condens. Matter Mater. Phys.*, 1983, **27**, 858–866.
33 H. Cao, C. Cantoni, A. F. May, M. A. McGuire, B. C. Chakoumakos, S. J. Pennycook, R. Custelcean, A. S. Sefat and B. C. Sales, *Phys. Rev. B:Condens. Matter Mater. Phys.*, 2012, **85**, 054515.
34 G. Li, B. Zhang, T. Baluyan, J. Rao, J. Wu, A. A. Novakova, P. Rudolf, G. R. Blake, R. A. de Groot and T. T. M. Palstra, *Inorg. Chem.*, 2016, **55**, 12912–12922.
35 T. M. McQueen, Q. Huang, V. Ksenofontov, C. Felser, Q. Xu, H. Zandbergen, Y. S. Hor, J. Allred, A. J. Williams, D. Qu, J. Checkelsky, N. P. Ong and R. J. Cava, *Phys. Rev. B:Condens. Matter Mater. Phys.*, 2009, **79**, 014522.
36 M. Kawai, F. Nabeshima and A. Maeda, *J. Phys.: Conf. Ser.*, 2018, **1054**, 012023.
37 G. J. Snyder, A. H. Snyder, M. Wood, R. Gurunathan, B. H. Snyder and C. Niu, *Adv. Mater.*, 2020, **32**, 2001537.
38 T. Zhu, Z. Xu, J. He, J. Shen, S. Zhu, L. Hu, T. M. Tritt and X. Zhao, *J. Mater. Chem. A*, 2013, **1**, 11589–11594.
39 Q. Zhang, F. Cao, W. Liu, K. Lukas, B. Yu, S. Chen, C. Opeil, D. Broido, G. Chen and Z. Ren, *J. Am. Chem. Soc.*, 2012, **134**, 10031–10038.
40 Q. Zhang, Z. Ti, Y. Zhu, Y. Zhang, Y. Cao, S. Li, M. Wang, D. Li, B. Zou, Y. Hou, P. Wang and G. Tang, *ACS Nano*, 2021, **15**, 19345–19356.
41 M. Li, S. M. Kazi Nazrul Islam, M. Yahyaoglu, D. Pan, X. Shi, L. Chen, U. Aydemir and X. Wang, *INFOMAT*, 2019, **1**, 108.

42 C. Zhou, Y. K. Lee, Y. Yu, S. Byun, Z.-Z. Luo, H. Lee, B. Ge, Y.-L. Lee, X. Chen, J. Y. Lee, O. Cojocaru-Mirédin, H. Chang, J. Im, S.-P. Cho, M. Wuttig, V. P. Dravid, M. G. Kanatzidis and I. Chung, *Nat. Mater.*, 2021, **20**, 1378–1384.

43 R. Dronskowski and P. E. Bloechl, *J. Phys. Chem.*, 1993, **97**, 8617.

44 S. Maintz, V. L. Deringer, A. L. Tchougréeff and R. Dronskowski, *J. Comput. Chem.*, 2016, **37**, 1030.

45 T. Katase, N. Sato and T. Mori, *Appl. Phys. Rev.*, 2025, **12**, 041319.

46 D. T. Morelli, V. Jovovic and J. P. Heremans, *Phys. Rev. Lett.*, 2008, **101**, 035901.

47 M. Dutta, K. Pal, U. V. Waghmare and K. Biswas, *Chem. Sci.*, 2019, **10**, 4905–4913.

48 N. Sato, N. Kuroda, S. Nakamura, Y. Katsura, I. Kanazawa, K. Kimura and T. Mori, *J. Mater. Chem. A*, 2021, **9**, 22660–22669.

49 X. He, S. Nomoto, T. Komatsu, T. Katase, T. Tadano, S. Kitani, H. Yoshida, T. Yamamoto, H. Mizoguchi, K. Ide, H. Hiramatsu, H. Kawaji, H. Hosono and T. Kamiya, *Adv. Funct. Mater.*, 2023, **33**, 2213144.

50 M.-H. Fang, H.-D. Wang, C.-H. Dong, Z.-J. Li, C.-M. Feng, J. Chen and H. Q. Yuan, *Europhys. Lett.*, 2011, **94**, 27009.

51 K. Momma and F. Izumi, *J. Appl. Crystallogr.*, 2011, **44**, 1272–1276.